Directional and Polarized Lasing Action on Pb-free FASnI$_3$ Integrated in Flexible Optical Waveguides

Isaac Suárez,* Vladimir S. Chirvony, Jesús Sánchez-Díaz, Rafael S. Sánchez,
Iván Mora-Seró,* and Juan P. Martínez-Pastor*

In this work, high-quality FASnI$_3$ (FA, formamidinium) lead-free perovskite thin films are successfully incorporated in a flexible polyethylene terephthalate (PET) substrate to demonstrate amplified spontaneous emission (ASE) and lasing. The waveguide (WG) consists of polymethylmethacrylate(PMMA)/FASnI$_3$ bilayer deposited on a PET substrate and is properly designed to allow single-mode propagation at the photoluminescence wavelength. This geometry optimizes the excitation of the emitting FASnI$_3$, enhances the light–matter interaction in the semiconductor thin film, provides a preferable direction for the emitted light and allows its direct outcoupling for on-chip or fiber-optic applications. As far as the authors know, ASE and random lasing are obtained for the first time in a flexible-based WG integrating a highly efficient lead-free perovskite. The high quality of the deposited films and the optimized design of the structure result in an extremely low ASE/lasing threshold in the range of 1 µJ cm^{-2}, which is only ten times higher than that measured in the same PMMA/FASnI$_3$ structure deposited on a rigid substrate (Si/SiO$_2$). More interestingly, these WGs exhibit a strong polarization anisotropy for the outcoupled ASE/lasing light with a preferable transverse electric polarization. This work is the base for the future development of ecofriendly, flexible, and efficient photonic devices.

1. Introduction

The development of a technology for flexible photonics (FP) has become one of the most important trends in the optoelectronics community for the 2020 decade.[1,2] A photonic circuit that can maintain a stable performance under mechanical deformation will give rise to a large spectrum of vanguardist applications, ranging from optical links[3] to wearable sensors directly in contact with skin or clothes.[4] As earlier proposed for flexible electronics,[5,6] one of the main goals of FP consists in reproducing previous achievements in rigid (silicon-based) micro(nano) photonic circuits on a flexible substrate. Successful examples include passive resonators,[7] plasmonic crystals,[8] optical amplifiers,[9] organic light emitting diodes or photodetectors.[10] In this scenario, the demonstration of stimulated emission in the FP device paves the road of much more advanced functionalities derived from the on-chip generation of coherent light. The common strategies to implement an optical amplifier or a laser on a given substrate consist of integrating a material with optical gain in Fabry–Perot, distributed feedback or whispering gallery mode resonators. However, to be effective these photonic structures need complicated fabrication methods, which become more challenging in the case of a flexible platform. Consequently, only a few publications developed the appropriate technology to demonstrate a reliable stimulated emission device on a flexible substrate.[11,12]

Ideally, a lasing flexible device should be fabricated by means of simple and straightforward technology, allowing an efficient coupling of the excitation beam together with directional light emission and efficient outcoupling. In this context, the outstanding optical properties of halide perovskites and their straightforward integration onto different substrates seem optimum for developing such a lasing flexible technology. Moreover, the use of nontoxic materials to be in contact with human skin or tissues should also be a requirement for the potential biomedical applications of this sort of future optoelectronic/photonic sensing devices.[13–16] Fortunately, lead-free perovskites (LFP) have opened promising routes for such a new generation of ecofriendly optical sources,[17] as an alternative to the lead halide perovskite (LP) families. Nevertheless, although

I. Suárez
Escuela Técnica Superior de Ingeniería
Universidad de Valencia
Valencia 46100, Spain
E-mail: isaac.suarez@uv.es
V. S. Chirvony, J. P. Martínez-Pastor
UMDO
Instituto de Ciencia de los Materiales
Universidad de Valencia
Valencia 46980, Spain
E-mail: juan.mtnez.pastor@uv.es
J. Sánchez-Díaz, R. S. Sánchez, I. Mora-Seró
Institute of Advanced Materials (INAM)
Universitat Jaume I
Castelló de la Plana
Castelló 12006, Spain
E-mail: sero@uji.es

LPs have been consolidated as excellent optical gain materials for traditional resonators[18–21] or random lasing (RL),[22] the use of LFPs for developing lasers or optical amplifiers is still at its infancy.[23] There are only few experimental works where amplified spontaneous emission (ASE) and/or lasing is demonstrated with Sn-based perovskites, particularly $MASnI_3$ (MA, methylammonium), $FASnI_3$ (FA, formamidinium), and $CsSnI_3$.[24–27] Nevertheless, the Sn-based perovskites demonstrate an extremely low stability in air environment,[28] and ASE was only observed under vacuum conditions. More importantly, it is still not solved how to stablish an efficient pumping of the LFP semiconductor and decouple the emitted light, which is mandatory in an integrated optical technology. This requirement makes it more difficult to implement ASE/lasing devices on flexible substrates and publications for such devices are absent literature.

In this manuscript, we demonstrate the production of ASE under a very low pulsed laser pumping threshold by incorporating a $FASnI_3$ film in the planar waveguide (WG) configuration illustrated in **Figure 1**. Low annealing temperature, 100 °C, used for the crystallization of $FASnI_3$, allows the deposition on polyethylene terephthalate (PET) substrate and represents an important breakthrough in low-temperature processing LFP nanomaterials. Moreover, although Sn-based LFPs present severe problems in terms of material stability,[29] we recently demonstrated that it is possible to increase notably the stability of these films by the use of appropriate additives and light soaking treatment.[30] In this way, our $FASnI_3$ films manifested a relatively good stability with an almost constant ASE intensity operation over more than 30 min at room temperature and ambient conditions. Improved stability and longer runtime experiments (2–3 h) were possible by using flowing N_2 on top of the device surface. The configuration of the WG consisted of a polymethylmethacrylate (PMMA)/$FASnI_3$ bilayer structure deposited on top of a flexible PET substrate. To clarify the constraints produced in the system using a flexible substrate, these WG structures on PET were compared with identical structures, but deposited on a rigid Si/SiO_2 substrate. The PMMA cladding layer of the WG enables an efficient pumping by the propagation of the excitation beam at 532 nm (green curve in Figure 1) end-fire coupled at the input edge of the WG, while the semiconductor thin film enhances the light-matter interaction due to the high confinement through the fundamental mode of the WG structure (red curve in Figure 1).[31,32] Here, an optimum thickness of 200 nm is chosen to allow single-mode propagation at the photoluminescence (PL) peak wavelength (890 nm) of $FASnI_3$ and to enhance the optical gain of the transverse electric (TE) polarization mode at the expense of the transverse magnetic (TM) one. Consequently, the device shows a preferable TE polarization for the emitted light in analogy to the III-V quantum well epitaxial lasers.[33] This interesting feature is, to the best of our knowledge, the first time that it has been reported in a bulk perovskite material and paves the road for applications where the polarization of the light is required, such as wavelength filtering or multiplexing.

The high quality of the fabricated $FASnI_3$ films and the benefits of the WG configuration are clearly demonstrated by enhanced light emission and efficient outcoupling. In the case of a flexible PET substrate the device shows an extraordinarily low threshold for ASE, ≈1 µJ cm^{-2}, which is much lower than values reported in literature for Sn-based perovskite thin films deposited on rigid substrates and using back-scattering
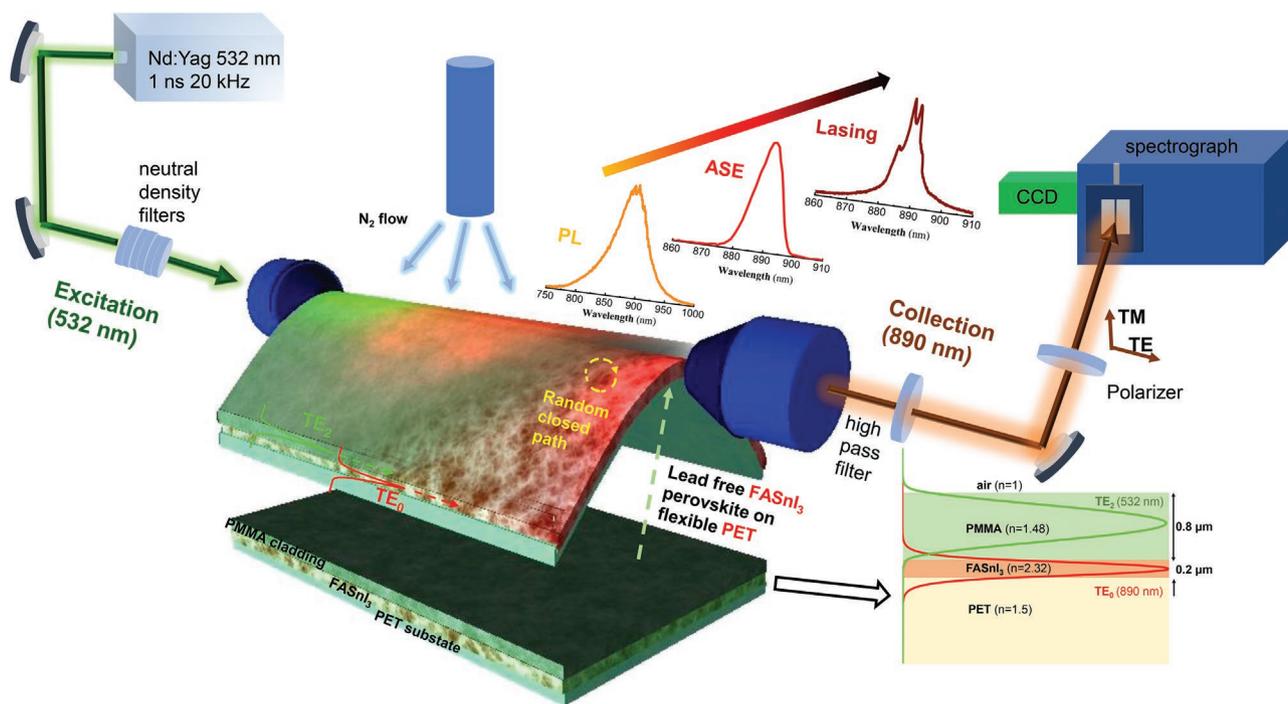
Figure 1. Scheme of the waveguide structure (center) and optical modes (bottom-right), the experimental setup (left and top-right) and waveguided emitted light spectra (top): PL, ASE and RL.

**ADVANCED
SCIENCE NEWS**
www.advancedsciencenews.com

**ADVANCED
OPTICAL
MATERIALS**
www.advopticalmat.de

geometry,[24–27] and also lower than those reported for MAPbI$_3$ films deposited on flexible substrates. Moreover, we obtained a lower ASE threshold of 100 nJ cm^{-2} in our FASnI$_3$-based WG structures prepared on rigid Si/SiO$_2$ substrates, which is not far from the best values we obtained for MAPbI$_3$ integrated in a similar WG geometry.[31,32] Moreover, we observed more fascinating results derived from the generation of narrow spikes in the ASE band that can be attributed to waveguided RL. Finally, the lasing/ASE generated in FASnI$_3$ flexible WGs was studied as a function of the convex curvature produced by mechanical bending applied to this device. We believe that present results will be the basis of new functionalities in future integrated silicon, flexible photonics, and wearable laser-based chips produced by using solution processed lead-free perovskites.

2. Optimum Configuration for ASE

FASnI$_3$ films were fabricated following the procedure detailed in the Experimental Methods section. The layers show a polycrystalline morphology with a grain size of 600–1000 nm, see SEM image in Figure S1 (Supporting Information), and a uniform thickness of ≈200 nm provided by the fabrication conditions, such as spincoating velocity and annealing temperature (4000 rpm and 100 °C, respectively, in the present work). In analogy with polycrystalline LP,[34] FASnI$_3$ films show a high absorption coefficient (> 10^5 cm^{-1}) below 600 nm, see Figure S2 (Supporting Information). Concretely, the band edge absorption at room temperature is located at ≈850 nm, and the absorption coefficient reaches approximate values of $\alpha_p = 17.08$ μm^{-1} and $\alpha_s = 0.216$ μm^{-1} at the pump (532 nm) and PL signal (890 nm) wavelengths, respectively. The PL spectrum is centered at 890 nm, orange line in Figure 1, which is characterized by a decay time of $\tau_d = 1.4\ ns$, see Figure S3 (Supporting Information). The reflectivity of the films deposited on silicon, see Figure S4 (Supporting Information), allows a good estimation of the real part of the refractive index for the FASnI$_3$ film with the phenomenological law $n = 2.6\ \exp(-10^{-4}\ \lambda)$, where λ is the wavelength in nm. This law for n was obtained from the best fitting of the calculated reflectivity using the transfer matrix method (TMM) to the experimental reflectivity.[35] This function gives a refractive index of ≈2.4 in the visible-IR range, which is consistent with reported values for this material.[36–38]

The WG configuration proposed in this work consists of a PMMA/FASnI$_3$ bilayer structure deposited on a flexible PET substrate, as illustrated in Figure 1, and the same structure fabricated on a SiO$_2$/Si substrate (2 μm of SiO$_2$) for benchmarking purposes of ASE (and lasing) action. The bilayer configuration has been chosen according to previous results obtained with polycrystalline MAPbI$_3$ films,[10,31,32] where we demonstrated the generation of ASE under extremely low thresholds (≈10 nJ cm^{-2}). Briefly, the proposed structure provides an efficient excitation of the active medium together with a strong light-matter interaction, which is due to the high electromagnetic confinement in the fundamental mode. For this purpose, the WG is defined by the refractive-index contrast (Δn) between its different layers of the structure and was modeled by a TMM algorithm.[35] According to the mode analysis developed for the PMMA/MAPbI$_3$/SiO$_2$ waveguide,[31] a perovskite

film thicker than 250 nm results in multimode propagation at the PL wavelength and the PMMA should be thicker than 0.5 μm to increase the propagation length of the pump beam at 532 nm (for 0.5 μm the effective absorption is ≈1 μm^{-1}).[31] Here, similar conclusions can be extracted, and the thicknesses of FASnI$_3$ and PMMA layers were fixed to $d_1 = 200$ nm and $d_2 = 600$–1000 nm, respectively, because these values optimize the propagation along with the WG of the pump beam at 532 nm and the emitted light at 890 nm, see section S2 (Supporting Information).

The excitation beam at 532 nm is end-fire coupled at the input edge of the WG and propagates along its entire length (1 mm) through the TE$_2$ (TM$_1$) cladding mode (see the green curve in the bottom-right inset of Figure 1 and Figure S5, Supporting Information), whose power distribution is mainly confined in the PMMA. At the same time, emitted light at 890 nm is excited along with the WG by the evanescent field of that mode, which has previously proved an efficient method.[31] In fact, the PL signal at 890 nm propagates through the TE$_0$ (TM$_0$) fundamental and unique mode of the WG structure (see the red curve in the bottom-right inset of Figure 1 and Figure S5, Supporting Information). In particular, the mode analysis indicates an effective refractive index higher for the TE$_0$ mode (higher confinement) in the LFP semiconductor and a preferable TE polarization for the emitted light. Besides, the overlap of emitted light with the active medium is a necessary condition to enhance stimulated emission. Consequently, above a relatively low threshold, our WG structure shows the spectrum-narrowing characteristic of ASE, the red spectrum in Figure 1, and the appearance of spikes typical of lasing, the brown spectrum in Figure 1. Furthermore, the WG configuration enables the direct end-fire outcoupling of waveguided PL or ASE signals.

3. ASE and RL in Rigid Waveguides

3.1. Generation of ASE and Lasing

A PMMA/FASnI$_3$ WG fabricated on a rigid SiO$_2$/Si substrate was prepared and measured for benchmarking purposes, see **Figure 2**a for the experimental laser-pumping/light-collection scheme and Figure 2b for a SEM cross-section image of the WG structure. When the excitation beam at 532 nm was end-fire coupled at the input edge of the WG, a bright PL line at 890 nm was decoupled at its output edge, as shown in the CCD image of Figure 2c. This outcoupled PL line corresponds to the near field distribution of the fundamental TE$_0$ mode of the WG, which is highly confined in the semiconductor film.

The waveguided PL spectrum demonstrates a progressive narrowing by increasing the excitation fluence (I), due to the production of ASE after a certain threshold, see Figure 2d. Moreover, in case of high excitation fluence, the ASE spectrum exhibits sharp peaks, which are a distinctive feature of lasing action (see inset in linear scale).[14,15] In fact, the log-log plot of the waveguided PL intensity (I_{PL}) as a function of fluence I shows the typical S-shaped curve characteristic of lasing action (hollow brown circles in Figure 2e), in parallel to the progressive reduction of the full width at half maximum (FWHM) of the
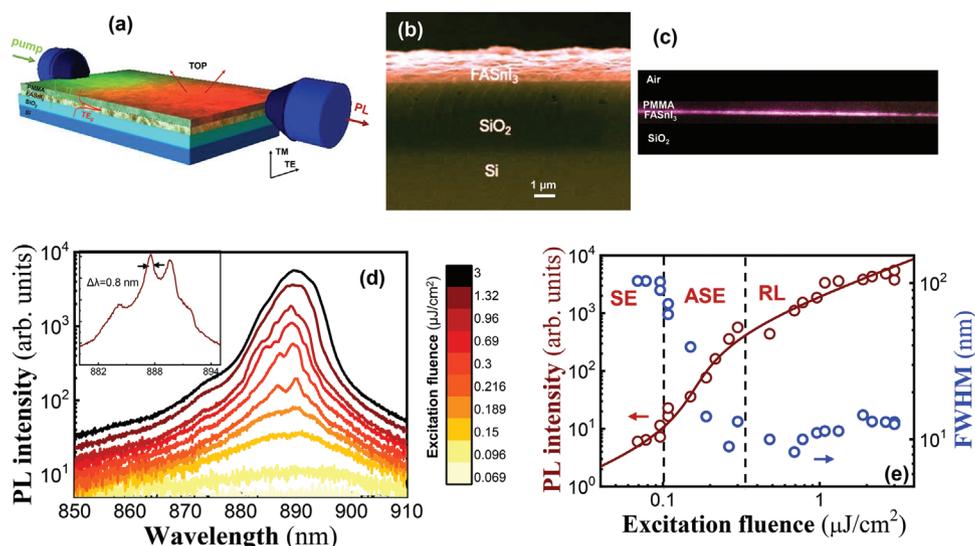
Figure 2. ASE and lasing on FASnI₃ rigid waveguide. a) Scheme of the sample. b) SEM cross section of the FASnI₃ film. c) TE₀ at 890 nm collected at the output edge of the WG. d) PL spectra for different excitation fluences. Inset show the detail of the lasing lines. e) PL peak intensity and FWHM as a function of the excitation fluence. Brown solid line corresponds to the modelling with a standard laser equation.

signal spectrum above the ASE threshold (hollow blue circles in Figure 2e). This dependence reveals three different regions separated by vertical dashed lines in Figure 2e. Region SE observed for I < 100 nJ cm⁻² where the PL spectrum is characterized by a Gaussian shape centered at 890 nm with a FWHM ≈100 meV (64 nm) that corresponds to the spontaneous emission of FASnI₃ due to exciton recombination at room T,[25] and hence exhibiting a linear variation with fluence, $I_{PL} \propto I$. Region ASE begins above a fluence threshold of ≈I ≈100 nJ cm⁻², where the spectrum of waveguided emitted light progressively collapses down to a narrow Lorentzian line of 10 meV (6.4 nm) that shows a superlinear increase ($I_{PL} \propto I^{3.2}$). This behavior is a clear signature of stimulated light emission and indicates the suitability of the proposed WG as optical amplifier. Indeed, the ASE threshold of 100 nJ cm⁻² measured here is about one order of magnitude higher than that found for MAPbI₃ films integrated in a similar WG configuration,[10,31,32] and significantly smaller than values reported for Sn-perovskite films pumped under backscattering geometry until now.[24–27] Finally, the RL region observed for I > 300 nJ cm⁻² is characterized again by a linear growth of I_{PL} with the excitation ($I_{PL} \propto I$) and the appearance of very narrow spikes (< 1 nm, see the inset in Figure 2d) over the already narrow ASE line, which is attributed to lasing action. Since there is not any integrated optical resonator within the WG, the lasing action is ascribed to the formation of random cavities, where a positive feedback is provided by the strong scattering in the polycrystalline grains.[26,39–41] Moreover, RL spectra collected at different zones of the rigid WG show different peak wavelengths, as depicted in Figure S6a (Supporting Information) (four different points). In this way, the statistics obtained over 200 RL lines indicate that the frequencies of their peak wavelengths exhibit a distribution consistent with the profile of the ASE spectrum, as observed in Figure S6b (Supporting Information). A Fast Fourier Transform procedure carried out with these spectra, Figure S6c–d (Supporting Information), indicates average cavity lengths in the range $L_c \approx 231$–244 µm,

which is consistent with that found for CsSnI₃[26] or MAPbI₃ thin films.[41] The benefit of our WG structure is given by such very low ASE/lasing thresholds (100/300 nJ cm⁻²), which are smaller than the RL reported for films of CsSnI₃ (18 mJ cm⁻²),[26] MAPbBr₃ (800 µJ cm⁻²),[42] MAPbI₃ (30–150 µJ cm⁻²),[41,43] CsPbBr₃ quantum dots (40 µJ cm⁻²)[44] and tin-based Ruddelsden–Popper perovskites (0.5–3 µJ cm⁻²),[45,46] all pumped under surface/backscattering excitation.

It is interesting to note that ASE/lasing lines broaden by increasing the excitation over 1 µJ cm⁻² producing the fusion of RL lines within the ASE shape. The broadening can be attributed to several mechanisms working separately or in different combinations: i) saturation effects caused by thermal heating; ii) the fact that the carrier density at such excitation fluences, [0.46–1.38]·10¹⁸ cm⁻³, has reached the Mott transition in the tin perovskite, ≈10¹⁸ cm⁻³, and the ASE becomes broader because of the influence of the electron-hole plasma;[31] iii) the fact that such a level of excitation is above the carrier density threshold where Auger recombination becomes non-negligible, 2.5·10¹⁷ cm⁻³;[47] and iv) a more important contribution of the waveguided extended modes responsible for the ASE compared to the (scattering-induced) localized modes responsible for narrow RL peaks.

The generation of stimulated emission in our WGs can be understood by the comparison of the experimental carrier density at threshold (N_0) and the theoretical value expected from the theory of semiconductor optical amplifiers.[31] On the one hand, the experimental carrier density (G) at low excitation fluences (below or close to threshold) can be estimated with the equation:

$$G(z) = \frac{I \cdot \alpha}{h\nu} \qquad (1)$$

where α is the absorption at the pump wavelength, I is the excitation fluence, and $h\nu$ is the excitation photon energy. At these conditions, the thresholds for the ASE and RL regimes

yield $N_0 = 4.5 \times 10^{16}$ cm^{-3} and $N_0 = 2 \times 10^{17}$ cm^{-3}, respectively. On the other hand, the theoretical threshold of optical gain in a semiconductor can be estimated from the transparency condition (gain = losses) through the electron (f_c) and hole (f_v) occupation probabilities, (i.e., $f_c = f_v = 0.5$).[31] By using the electron and hole effective masses for FASnI$_3$, $m_e = 0.28 \, m_0$ and $m_h = 0.11 \, m_0$, respectively,[48] the transparence carrier density at threshold (N_{th}) reaches the value $N_{th} = 1.34 \times 10^{18}$ cm^{-3}. The large difference between the experimental values of N_{th} and N_0 can be ascribed to the benefits induced by the optical WG structure, which leads to an enhancement of emitted light by the coupling to a given optical mode.[49] Indeed, the transparent concentration for ASE, $N_0 = 4.5 \times 10^{16}$ cm^{-3}, is smaller than previously reported values for FASnI$_3$ films excited under femtosecond laser pulses at 800 nm,[25] and close to that obtained in MAPbI$_3$ films integrated in similar WG geometry.[31] Considering the experimental transparency for RL $N_0 = 2 \cdot 10^{17}$ cm^{-3}, $\alpha_p = 17.08$ µm^{-1} and $\tau_r = 1.4$ ns measured for our FASnI$_3$ films and the mode analysis described in S2 (Supporting Information), the variation of the emission intensity with the laser fluence can be nicely reproduced with the standard semiconductor laser model (solid brown line in Figure 2e), as described in section S4 (Supporting Information).[50] The optical gain (g), transient time of the photons in the cavity (τ_c), and the spontaneous emission factor (β), are the figures of merit that can be extracted from this model to fit the experimental lasing curve (hollow brown circles in Figure 2e). The WG structure based on FASnI$_3$ in the present work yield $g = 1600$ cm^{-1}, which corresponds to a material gain of 2000 cm^{-1} and a net gain of 23 cm^{-1} averaged along the whole length of the structure (1 mm). Besides, the model suggests a photon lifetime in the cavity $\approx \tau_c = 2$–3 ps and a spontaneous emission factor $\beta = 0.70$.

The parameter β represents the fraction of the spontaneously emitted light that is coupled to the lasing/amplified mode. The aleatory paths characteristic of a standard random laser usually results in a limited value of β. For example, theoretical studies predict that this factor is limited to $\beta = 0.1$ in a generic random laser[51] or $\beta = 0.04$ in a random laser based on MIE resonances.[52] Similar values have been obtained experimentally in a suspension of TiO$_2$ nanoparticles inside a dye solution, $\beta = 0.07$,[53] in a Nd:LuVO4 crystal powder, $\beta = 0.18$,[54] and MAPbBr$_3$ perovskite film deposited on PET, $\beta = 0.14$.[55] These low values of β are usually correlated with high RL thresholds ($\approx$mJ cm^{-2}). Nevertheless, this parameter can be enhanced by providing some directionality for the RL light, for example by using a disordered photonic crystal waveguide, where $\beta = 0.31$,[56] or the present result, $\beta = 0.7$. Such a high value of β indicates that most of the emitted light is coupled to the lasing mode attributable to the strong electromagnetic field confinement in the waveguide, also leading to the measured low ASE/RL thresholds of $\approx$100/300 nJ cm^{-2}.

3.2. Stability, Directionality, and Polarized Emission

Beyond the optical effect, the PMMA cladding serves as a protective layer against water or oxygen moisture and hence enhancing the stability of Sn-based perovskite.[32] As a result, the evolution of ASE spectra in the FASnI$_3$-based WG as a function of time shows only small changes in the linewidth and intensity of the RL lines. The recorded waveguided PL at 0 s, **Figure 3**a, and 1500 s, Figure 3b, presents the same RL wavelengths with a slight broadening/narrowing of the linewidth, and almost constant intensity, see the map in Figure 3c. The
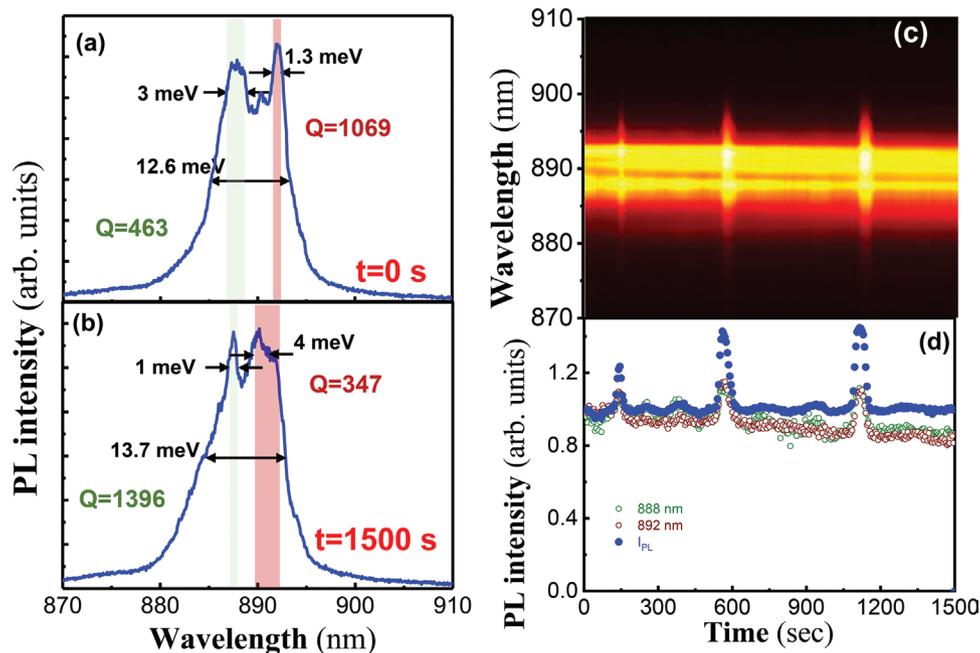
Figure 3. Evolution of the RL action during the time in a rigid substrate. a) Spectra at $t = 0$. b) Spectra at $t = 1500$ s. c) Map of the PL spectra as a function of the time. d) Evolution of the integrated PL intensity of the ASE band (I_{PL}) and the RL peak intensity at 888 nm (green symbols) and 892 nm (brown symbols), all normalized at $t = 0$.
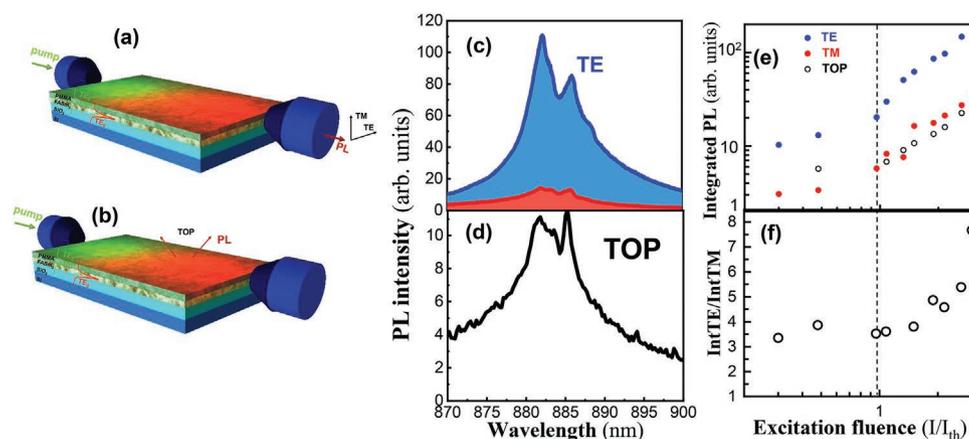
Figure 4. Experimental configuration to measure: a) Waveguided TE/TM PL, b) TOP emitted PL. RL spectra were collected in c) TE/TM polarization, d) surface of the sample (TOP). e) Integrated PL intensity. Blue, red and open symbols correspond to TE, TM, and TOP, respectively. f) Ratio of the integrated intensities in TE and TM polarizations as a function of the I.

peak intensity of the RL lines and the integrated intensity of the whole ASE band exhibit a variation lower than 30% of the average value, see Figure. 3d. The more or less periodic fluctuations observed at 150, 600, and 900 s can be explained by variations of the RL threshold.[14] This behavior is characteristic of a random laser system when the excitation pulse duration is comparable to or longer than the spontaneous PL lifetime,[51] which is the case of the $FASnI_3$ waveguide used in this work.

Although emitted light produced by exciton recombination is initially omnidirectional, the WG configuration selects a preferable momentum for the emitted light parallel to the TE_0 mode, which stablishes a directional extraction of light from the output edge of the WG and appropriate outcoupling to a fiber optic (**Figure 4**a) or on-chip devices. Figure 4 compares ASE light collected in the TE (blue), TM (red), and TOP (black) directions, using the experimental configurations depicted in Figures 4a–b. The three collection conditions show a similar spectrum (Figures 4c–d) and laser fluence threshold (Figure 4e), being the outcoupled emitted light much more intense along the WG direction. In particular, the emission of the film shows a preferential TE polarization. For spontaneous emission, the ratio $I_{TE}/I_{TM} \approx 3.5$, while it grows more than 100%, $I_{TE}/I_{TM} > 7$, above the ASE threshold (at the maximum excitation power), as shown in Figure 4f.

Again, it is worth mentioning that the directionality provided by the WG represents a cheap and elegant way to increase the signal-to-noise ratio and provide a direct outcoupling of laser light from the WG without expensive technology or complicated pump systems.[52–57] Moreover, the outcoupled RL light from the WG is polarized parallel to the TE polarization, which is observed for the first time in perovskite thin films, to the best of our knowledge, but previously observed in ZnO thin films,[58] in liquid crystals[59] or plasmonic systems.[60]

4. ASE and Lasing in Flexible Waveguides

One of the many advantages of LPs is their extraordinary optical and electrical quality in polycrystalline form, leading to very efficient optoelectronic and photonic devices, even fabricated

on flexible substrates.[61] It is important to say that the demonstration of optoelectronic functionalities in flexible structures is always challenging due to the particular technique used for deposition and the film formation (and adhesion) on a plastic substrate, other than its posterior behavior under mechanical strain and deformation conditions. These limitations could be eventually more important in the case of Sn-based LFPs, because their films can exhibit pinholes and poor stability under ambient conditions, even if they are deposited on rigid substrates.[28] Contrarily, this is not the case for our $FASnI_3$ layers,[30] see Experimental Methods for further details of thin film fabrication. This success is the basis for expecting good results with optical WGs fabricated on flexible substrates, particularly PET, one of the most used in the market for many applications. In analogy to the rigid structure, the flexible WGs also allows the simultaneous propagation of the excitation beam at 532 nm and the emitted light signal at 890 nm through the TE_2 and TE_0 (TM_0) modes of the WG (S2, Supporting Information), respectively, which can be decoupled at the WG output edge as shown in the image of **Figure 5**a.

ASE and narrow RL lines are also observed by increasing sufficient excitation fluence, as shown in Figure 5b, similarly to the WG fabricated on Si/SiO_2. The evolution of I_{PL} and FWHM of outcoupled light spectra with the excitation laser fluence is shown in Figure 5c (brown and blue solid circles, respectively). The ASE/RL thresholds derived from the superlinear increase of I_{PL} and the narrowing of the FWHM are $\approx 1.5/3$ μJ cm^{-2}. These values are one order of magnitude higher than those found for our best benchmark lead-free perovskite device fabricated on the Si/SiO_2 substrate (100 nJ cm^{-2}). This difference can be correlated with the different decay time measured under similar conditions in the $FASnI_3$ film spincoated on Si/SiO_2 (see Figure S3, Supporting Information of the revised Suppl. Information) and PET (see Figure S7, Supporting Information): the decay time is ≈ 0.5 ns for the PET sample, as compared to 1.4 ns in the reference Si/SiO_2. This means a more important influence of nonradiative recombination for $FASnI_3$ on PET, hence explaining the observed increase in its ASE/RL thresholds. The worse quality in this case may be attributable to different grain nucleation, dislocation concentration, and adhesion to the substrate.
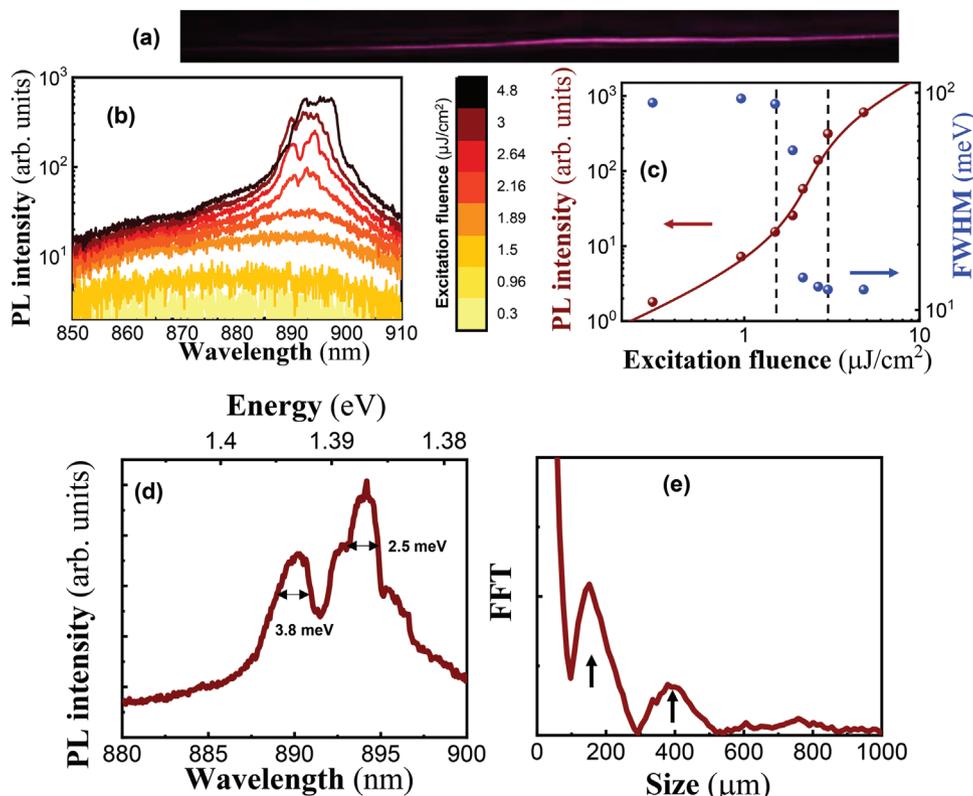
Figure 5. ASE and RL on FASnI$_3$ a flexible waveguide. a) TE$_0$ at 890 nm collected at the output edge of the WG. b) PL spectra for different excitation fluences. c) PL intensity and FWHM as a function of the excitation fluence. Brown solid line corresponds to the modeling with a standard laser equation. d) Zoom of the RL emission. e) FFT of the RL spectra in Figure 5d.

In spite of the lower quality of FASnI$_3$ on PET, the values of ASE/RL thresholds found in the present work (1.5/3 μJ cm^{-2}) are still remarkably lower than values reported for other semiconductor materials. For example, a typical RL threshold of ≈1 mJ cm^{-2} is usually reported for dyes[13,15] or colloidal quantum dots,[60,62] in both cases prepared as thin films on rigid substrates. In the case of LPs, the threshold of RL is reduced down to 1–10 μJ cm^{-2} in the case of thin films deposited on rigid substrates,[41,42,44,45,63,64] but it increases up to 0.1–1 mJ cm^{-2} for similar films on flexible ones (polyimide, Ni foam).[40,65] Moreover, a threshold as high as 10 mJ cm^{-2} was reported for a tin-perovskite deposited on (rigid) mica.[26]

The reported threshold for FASnI$_3$ on PET is now taking place for a transparent carrier density (Equation 1 in section S4, Supporting Information) $N_0 = 6 \cdot 10^{17}$ cm^{-3}, by considering the experimental values of $\alpha_p = 17.1$ μm^{-1} and $\tau_r = 1.4$ ns for our FASnI$_3$ perovskite. In this way, the I_{PL}-I curve in Figure 5c can be nicely fitted with the standard lasing rate equation model, see section S4 (Supporting Information), by including a non-radiative decay rate of $A_{nr} = 1.3$ ns^{-1}, which may possibly be associated to a higher density of point or linear defects in the film deposited on PET.[66] Indeed, the recombination measured for the FASnI$_3$ films deposited on PET decreased from 1.4 ns down to 0.5 ns (see Figure S7, Supporting Information), which can be model by $A_r + A_{nr} = 1/0.5$ ns^{-1}, where $A_r = 1/\tau_r = 0.7$ ns^{-1}. Interestingly, the figures of merit extracted with the lasing rate equation model, see section S4 (Supporting Information), are: net gain of 23 cm^{-1}, a cavity time $\tau_c = 3$ ps and spontaneous emission factor of $\beta = 0.7$, that is, the same β found for the FASnI$_3$ WG fabricated on Si/SiO$_2$. The analysis of RL lines indicates a linewidth of ≈2.5–3.8 meV (1.6–2.4 nm), as observed in Figure 5d, which would correspond to a quality factor Q = 370–550. The corresponding FFT, see Figure 5e, exhibits Fourier harmonics located at $d_1 = 152$ μm and $d_2 = 386$ μm, again close to the values found in the rigid WG (see section S3, Supporting Information). The time evolution of the waveguided emitted light spectra under operational conditions in the ambient atmosphere (N$_2$ flowing on top of the WG) indicates good stability of the RL lines, because only small changes are observed in the linewidth, see Figures S8a–b (Supporting Information), and intensity, see Figures S8c–d (Supporting Information). In fact, we have measured light emission spectra in similar samples (FASnI$_3$ on PET) under backscattering geometry, where clear and intense RL lines are observed within small excitation regions of ≈100 μm^2 (Figure S10, Supporting Information). Finally, our flexible WGs still provide good directionality and a strong preferential polarization of outcoupled ASE/RL light, with 86% of the total intensity in TE polarization, as shown in Figure S10 (Supporting Information).

Finally, the ASE/RL emission is analyzed as a function of the convex bending curvature of the substrate, c, in order to establish the limits of the flexible device under practical operation, i.e., subjected to a certain mechanical bending condition. **Figure 6**a illustrates the experimental set-up scheme used to characterize the WG on the curved substrate and Figure S11 (Supporting Information) shows a photograph used to calculate

**ADVANCED
SCIENCE NEWS**

www.advancedsciencenews.com

**ADVANCED
OPTICAL
MATERIALS**

www.advopticalmat.de
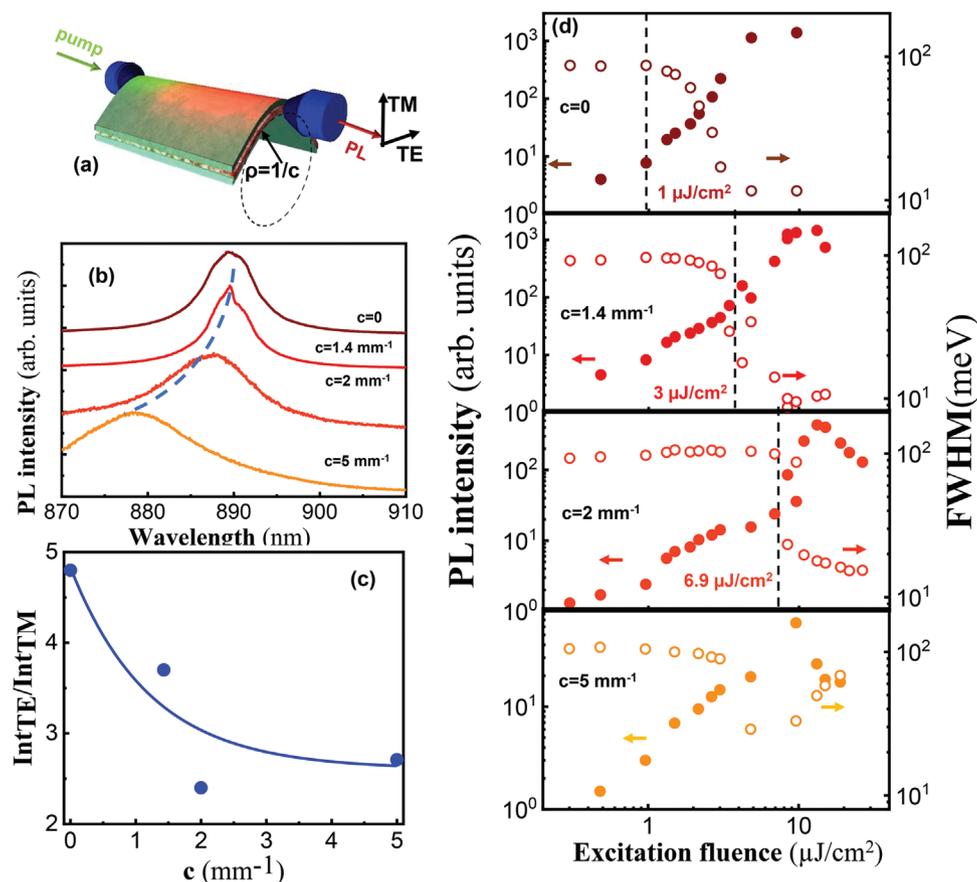
Figure 6. Analysis of the ASE/RL performances with the curvature. a) Scheme of the excitation/collection under bending. b) PL spectra for TE polarization above threshold with different curvatures. c) Ratio of TE/TM intensities. The blue line is a guide for the eye. d) Log–log plot of the I_{PL} (closed symbols) and FWHM (open symbols) as a function of I for TE polarization and the different curvatures.

the bending radius (ρ). In particular, we compared the performances of flat substrate ($c = 0$) with several bending radius $\rho = 0.2$, 0.4, and 0.7 cm corresponding to curvatures $c = 1.4$, 2, and 5 cm^{-1}. The emission spectra above threshold (> 2 μJ cm^{-2}) for the different curvatures are plotted in Figures 6b for TE polarization (TM shows a similar spectra). For flat substrates or small bends ($c = 1.4$ mm^{-1}) the PL consists of an ASE band centered at 890 nm with a FWHM ≈ 10 nm and containing the RL narrow spikes, as previously observed in Figure 5b and also in the benchmark devices. For higher bending curvatures ($c = 2$–5 mm^{-1}), however, the ASE band broadens up to 27 nm, RL-lines are no longer observed in the range of excitation fluences used in the experiments and shows, on average, a progressive blueshift, see dashed line in Figure 6b.

It is interesting to note here that the applied bending produces uniaxial compression along the radial direction (ρ) and biaxial tensile strain in the azimuthal direction, hence the observed blue shift observed for ASE would mean that it can be determined by the increase of the bandgap energy due to the biaxial tensile strain in the radial direction, similar to the observation with strained perovskites[67,68] or III-V quantum well lasers.[33] This effect deserves to be investigated with more detail in next future.

The increase of the ASE threshold with the mechanical bending is ascribed here to a shorter nonradiative exciton

recombination time, possibly associated to a higher dislocation concentration and/or pinholes in grain boundaries by increasing the layer strain conditions produced by the bending,[69] or the opening of more nonradiative channels associated to cracking, breakage or even exfoliation/detaching.[9,70]

The analysis of the ratio between the TE and TM intensities (I_{TE}/I_{TM}) indicates that the preferable polarization effect decreases with the curvature from $I_{TE}/I_{TM} = 4.8$ ($c = 0$) to $I_{TE}/I_{TM} = 2.7$ ($c = 5$ mm^{-1}), as shown in Figure 6c, i.e., at the level of the polarization ratio measured for spontaneous emission in the reference WGs fabricated on rigid substrates (figure 4f). Interestingly, this effect can be useful for applications where the tunning of the polarization degree would be needed, such as filtering, multiplexing, or bending sensors. The log-log plots in Figure 6d contain the evolution for I_{PL} and FWHM of the outcoupled waveguided emitted light as a function of the laser fluence for the flat substrate ($c = 0$) and three bending conditions. Clearly, the threshold (E_{th}), indicated in the Figure 6d with a dashed line, increases with the curvature from 1 μJ cm^{-2} ($c = 0$) to 7 μJ cm^{-2} ($c = 2$ mm^{-1}). For $c = 5$ mm^{-1} (very high convex bending) the I_{PL} intensity does not show a clear transition between a linear and superlinear dependence, even if the linewidth exhibits a decrease at fluences in the order of 10 μJ cm^{-2} (similar to the threshold for $c = 2$ mm^{-1}).

**ADVANCED
SCIENCE NEWS**

www.advancedsciencenews.com

**ADVANCED
OPTICAL
MATERIALS**

www.advopticalmat.de

Lastly, it is worth mentioning that the bending effect on ASE was perfectly reversible during the duration of the experiments. The characterization of the waveguides under mechanical bending was performed in different samples, in different points of the same sample and forward-reverse of convex bending conditions in the range $c = 0$ to $c = 5$ mm^{-1}, approximately, and back to $c = 0$. The samples always demonstrated similar ASE spectra under the same c with threshold ranging in the range 1–5 µJ cm^{-2} and a FWHM ≈ 8 nm (see Figure S12, Supporting Information). Only slightly different ASE thresholds and RL peak wavelengths were found in our experiments and ascribed to a different coupling efficiency or RL paths rather than sample damage of the sample during the mechanical bending experiments. Of course, multiple bending processes, convex-concave, and other mechanical deformations are needed to complete this study in the measure the stability of the tin-perovskite will be increased to develop much longer experimental runs.

5. Conclusions

In this manuscript, we successfully exploit the excellent emission properties of lead-free perovskite thin films to implement waveguide laser devices with an extremely low threshold and reasonably good stability. In particular, a PMMA/FASnI$_3$ bilayer is used as the cladding/core of a WG structure on both rigid SiO$_2$/Si and flexible PET substrates. These WGs enhance the generation of stimulated emission by an efficient pumping and strong light-matter interaction at the semiconductor thin film. As a result, the emitted light signal decoupled at the output of the rigid WG device showed ASE above ≈ 100 nJ cm^{-2}, close to the thresholds reported with perovskite materials containing Pb and this significantly improves previous results obtained with Pb-free perovskites. Similarly, WGs implemented on PET substrates exhibit a threshold in the range of 1 µJ cm^{-2}, which is a value much better than those reported in flexible devices based on Pb-perovskites and represents the first time where the optical gain is demonstrated for a flexible device based on a lead-free perovskite. Moreover, the intensity of the emitted light outcoupled from tin-perovskite WGs exhibit a S-shape as a function of the excitation fluence, which is characteristic of lasing operation together with the appearance of narrow spikes. These intensity spikes were attributed to the formation of RL loops caused by the strong scattering in the polycrystalline grains. A standard rate equation lasing model properly reproduces that S-shape for the WG outcoupled light, from which we deduce a β-parameter as high as 0.70, indicating that most of the emitted light is coupled to the lasing mode. Consequently, the WG configuration imposes a preferable directionality for the emitted light reducing the ASE threshold and allowing the formation of localized loops with high Q factors (Q > 1000) and narrow random lasing lines (< 1 nm). More importantly, the ASE/lasing light outcoupled from the WG shows a preferable TE lasing polarization, which is a particular signature of the high electromagnetic confinement in the WG, in contrast to the case of a bulk perovskite laser, where the emitted light is usually isotropic. Furthermore, the flexible WG continues to operate under mechanical bending conditions, demonstrating that ASE threshold, its peak wavelength, and the polarization ratio

I_{TE}/I_{TM} ratio, can be tuned with the curvature radius imposed to the PET substrate. We believe that the proposed device can be used in future sensing and telecommunication applications and represents an important step toward the development of a future cheap and ecofriendly perovskite flexible/wearable technology. Future work will address the study of similar devices after multiple bending processes, convex-concave, and other deformations in the measure. We will be able to increase the stability of the material to develop much longer experimental runs.

6. Experimental Section

Fabrication Procedure: Tin (II) iodide (SnI$_2$, 99.99%), tin(II) fluoride (SnF$_2$, 99%), N,N-dimethylformamide (DMF, 99.8%) and dimethylsulfoxide (DMSO, 99.8%) were purchased from sigma-aldrich. Formamidinium iodide (FAI. 99.99%) was purchased from Greatcell Solar Materials. These materials were used as received with no further purifications.

Dipropylammonium iodide salt was synthesized with the following procedure.[7] 10 g of dipropylamine was added to 30 mL of cold EtOH. Then 13 mL of HI was added dropwise to the flask under vigorous stirring. The white solid formed after the addition of HI was filtered and washed with 100 mL of cold diethylether and it was recrystallized using EtOH.

To prepare the FASnI$_3$ precursor solution, 298 mg of SnI$_2$ (0.8M), 123.8 mg of FAI (0.72M), 36.65 mg of DipI (0.16 M), 1.9 mg of NaBH$_4$ (0.05 M) and 12.48 mg of SnF$_2$(0.08 M) were dissolved in 1 ml of a mix solution of DMSO:DMF (9:1, v/v) and stirred over night at room temperature. After the fabrication process, a 3-day light soaking treatment was made inside a N$_2$ filled glovebox, using a white LED lamp, following our previous results on the beneficial effect of additives and light soaking.[30]

The different substrates (quartz, Si, SiO$_2$/Si or PET) were washed with ethanol, acetone, and isopropanol, respectively in a ultrasonic bath for 5 min each. After the wash, the substrates were dried with N$_2$ flux, and right before the perovskite film, they were treated with UV-Ozone for 20 min. The perovskite film was deposited by one step antisolvent method, by spin-coating at 4000 rpm a FASnI$_3$ precursor solution for 50 s and 400 µl of Chlorobenzene for 20 s, followed by an annealing at 70 °C and 100 °C for 1 min and 19 min, respectively. Finally, the PMMA solution (100 mg mL^{-1}) was spin-coated on top of the perovskite film at 3000 rpm for 30 s and baked at 70 °C for 1 min and 100 °C for 4 min. In the waveguide structures (SiO$_2$/Si and PET substrates) the samples are cleaved for characterization using end-fire coupling of the excitation laser.

Optical Characterization: Waveguides were characterized by end fire coupling a Nd:YAG laser doubled to 532 nm (1-ns pulses at 1-kHz repetition rate) at the input edge of the sample with the aid of a 40 × microscope objective mounted on an XYZ stage. The intensity of the excitation beam is controlled by neutral density filters. Waveguided photoluminescence (PL) was collected at the output edge of the sample with a 20 × microscope objective, also mounted on an XYZ stage. The outcoupled waveguide PL signal was collected, after a 550 nm long-pass filter and a linear polarizer, with the aid of a cylindrical lens and dispersed by a grating spectrograph (DNS-300 from DeltaNu) and detected by a back-illuminated Si CCD (DV420A-OE from Andor) at its exit.

Absorption measurements were carried out by using a commercial spectrofluorometer (HP8453 UV–VIS from Mettler) on a 200 nm FASnI$_3$ film deposited on quartz. The Reflectivity of a FASnI$_3$ film deposited on Si was measured by means of a commercial reflectometer (NanoCalc-2000 from Mikropack) to extract the refractive index of the film.

Supporting Information

Supporting Information is available from the Wiley Online Library or from the author.

Acknowledgements

Conflict of Interest

The authors declare no conflict of interest.

Data Availability Statement

The data that support the findings of this study are available from the corresponding author upon reasonable request.

Keywords

[1] Y. Bonnassieux, C. J. Brabec, Y. Cao, T. B. Carmichael, M. L. Chabinyc, K. Cheng, G. Cho, A. Chung, C. L. Cobb, A. Distler, *Flex. Print. Electron.* **2022**, *6*, 023001.

[2] S. Geiger, J. Michon, S. Liu, J. Qin, J. Ni, J. Hu, T. Gu, N. Lu, *ACS Photonics* **2020**, *7*, 2618.

[3] E. Bosnian, G. Van Steenberge, B. Van Hoe, J. Missinne, J. Vanfleteren, P. Van Daele, *IEEE Photonics Technol. Lett.* **2010**, *22*, 287.

[4] Y. Jin, G. Chen, K. Lao, S. Li, Y. Lu, Y. Gan, Z. Li, J. Hu, J. Huang, J. Wen, H. Deng, M. Yang, Z. Chen, X. Hu, B. Liang, J. Luo, *npj Flex. Electron.* **2020**, *4*, https://doi.org/10.1038/s41528-020-00090-9.

[5] G. C. Righini, J. Krzak, A. Lukowiak, G. Macrelli, S. Varas, M. Ferrari, *Opt. Mater. (Amst).* **2021**, *115*, 111011.

[6] P. Wang, M. Hu, H. Wang, Z. Chen, Y. Feng, J. Wang, W. Ling, Y. Huang, *Adv. Sci.* **2020**, *7*, 2001116.

[7] L. Li, H. Lin, S. Qiao, Y. Zou, S. Danto, K. Richardson, J. D. Musgraves, N. Lu, J. Hu, *Nat. Photonics* **2014**, *8*, 643.

[8] A. Espinha, C. Dore, C. Matricardi, M. I. Alonso, A. R. Goñi, A. Mihi, *Nat. Photonics* **2018**, *12*, 343.

[9] I. Suárez, E. Hassanabadi, A. Maulu, N. Carlino, C. A. Maestri, M. Latifi, P. Bettotti, I. Mora-Seró, J. P. Martínez-Pastor, *Adv. Opt. Mater.* **2018**, *6*, 1800201.

[10] J. K. Song, M. S. Kim, S. Yoo, J. H. Koo, D. H. Kim, *Nano Res.* **2021**, *14*, 2919.

[11] C. Zhang, C. L. Zou, Y. Zhao, C. H. Dong, C. Wei, H. Wang, Y. Liu, G. C. Guo, J. Yao, Y. S. Zhao, *Sci. Adv.* **2015**, *1*, https://doi.org/10.1126/sciadv.1500257.

[12] M. Karl, J. M. E. Glackin, M. Schubert, N. M. Kronenberg, G. A. Turnbull, I. D. W. Samuel, M. C. Gather, *Nat. Commun.* **2018**, *9*, 1525.

[13] A. S. L. Gomes, A. L. Moura, C. B. de Araújo, E. P. Raposo, *Prog. Quantum Electron.* **2021**, *78*, 100343.

[14] D. S. Wiersma, *Nat. Phys.* **2008**, *4*, 359.

[15] F. Luan, B. Gu, A. S. L. Gomes, K.-T. Yong, S. Wen, P. N. Prasad, *Nano Today* **2015**, *10*, 168.

[16] L. Sznitko, J. Mysliwiec, A. Miniewicz, *J. Polym. Sci. Part B Polym. Phys.* **2015**, *53*, 951.

[17] X. Li, X. Gao, X. Zhang, M. Shen, M. Lu, J. Wu, Z. Shi, V. L. Colvin, J. Hu, X. Bai, W. W. Yu, Y. Zhang, *Adv. Sci.* **2021**, *8*, 2003334.

[18] R. Wang, J. Wang, S. Tan, Y. Duan, Z. K. Wang, Y. Yang, *Trends Chem* **2019**, *1*, 368.

[19] F. Zhang, Z. Ma, Z. Shi, X. Chen, D. Wu, X. Li, C. Shan, *Energy Mater. Adv.* **2021**, *2021*, 1.

[20] Z. Liu, S. Huang, J. Du, C. Wang, Y. Leng, *Nanophotonics* **2020**, *9*, 2251.

[21] L. Lei, Q. Dong, K. Gundogdu, F. So, *Adv. Funct. Mater.* **2021**, *31*, 2010144.

[22] T. S. Kao, Y. H. Hong, K. Bin Hong, T. C. Lu, *Nanotechnology* **2021**, *32*, 282001.

[23] E. V. Ushakova, S. A. Cherevkov, V. A. Kuznetsova, A. V. Baranov, *Materials (Basel).* **2019**, *12*, https://doi.org/10.3390/ma122333845.

[24] P. Ščajev, R. N. Aleksiejū Nas, P. Baronas, D. Litvinas, M. Kolenda, C. Qin, T. Fujihara, T. Matsushima, C. Adachi, S. Juršėnas, *J. Phys. Chem. C* **2019**, *123*, 19275.

[25] R. L. Milot, G. E. Eperon, T. Green, H. J. Snaith, M. B. Johnston, L. M. Herz, *J. Phys. Chem. Lett.* **2016**, *7*, 4178.

[26] H. C. Hsu, Z. Y. Wu, Y. Y. Chen, L. J. Lin, *J. Phys. Chem. C* **2021**, *125*, 5180.

[27] G. Xing, M. H. Kumar, W. K. Chong, X. Liu, Y. Cai, H. Ding, M. Asta, M. Grätzel, S. Mhaisalkar, N. Mathews, T. C. Sum, *Adv. Mater.* **2016**, *28*, 8191.

[28] W. F. Yang, F. Igbari, Y. H. Lou, Z. K. Wang, L. S. Liao, *Adv. Energy Mater.* **2020**, *10*, 1902584.

[29] L. Lanzetta, T. Webb, N. Zibouche, X. Liang, D. Ding, G. Min, R. J. E. Westbrook, B. Gaggio, T. J. Macdonald, M. S. Islam, S. A. Haque, *Nat. Commun.* **2021**, *12*, 2853.

[30] I. M.-S. Sanchez-Diaz, R. S. Sánchez, S. Masi, M. Krečmarová, A. O. Alvarez, E. M. Barea, J. Rodriguez-Romero, V. S. Chirvony, J. F. Sánchez-Royo, J. P. Martinez-Pastor, *Joule* **2021**, https://doi.org/10.1016/j.joule.2022.02.014.

[31] I. Suárez, E. J. Juárez-Pérez, V. S. Chirvony, I. Mora-Seró, J. P. Martínez-Pastor, *Phys. Rev. Appl.* **2020**, *13*, 064071.

[32] I. Suárez, E. J. Juárez-Pérez, J. Bisquert, I. Mora-Seró, J. P. Martínez-Pastor, *Adv. Mater.* **2015**, *27*, 6157.

[33] M. J. Conelly, *Semiconductor Optical Amplifiers* **2002**.

[34] S. De Wolf, J. Holovsky, S. J. Moon, P. Löper, B. Niesen, M. Ledinsky, F. J. Haug, J. H. Yum, C. Ballif, *J. Phys. Chem. Lett.* **2014**, *5*, 1035.

[35] G. Lifante, *Integrated Photonics : Fundamentals*, **2002**.

[36] J. P. Correa-baena, H. Míguez, *J. Mater. Chem. A* **2016**, *4*, 11214.

[37] K. Ghimire, D. Zhao, Y. Yan, N. J. Podraza, *AIP Adv.* **2017**, *7*, 075108.

[38] R. Sabetvand, M. E. Ghazi, M. Izadifard, *J. Comput. Electron.* **2020**, *19*, 70.

[39] J. Yang, Z. Liu, M. Pi, H. Lin, F. Zeng, Y. Bian, T. Shi, J. Du, Y. Leng, X. Tang, *Adv. Opt. Mater.* **2020**, *8*, 2000290.

[40] Y. C. Wang, H. Li, Y. H. Hong, K. Bin Hong, F. C. Chen, C. H. Hsu, R. K. Lee, C. Conti, T. S. Kao, T. C. Lu, *ACS Nano* **2019**, *13*, 5421.

[41] R. Dhanker, A. N. Brigeman, A. V. Larsen, R. J. Stewart, J. B. Asbury, N. C. Giebink, *Appl. Phys. Lett.* **2014**, *151112*, https://doi.org/10.1063/1.4898703.

[42] Y. Liu, W. Yang, S. Xiao, N. Zhang, Y. Fan, G. Qu, Q. Song, *ACS Nano* **2019**, *13*, 10653.

[43] A. Safdar, Y. Wang, T. F. Krauss, *Opt. Express* **2018**, *26*, A75.

[44] X. Li, Y. Wang, H. Sun, H. Zeng, *Adv. Mater.* **2017**, *29*, 1701185.

[45] P. K. Roy, R. K. Ulaganathan, C. M. Raghavan, S. M. Mhatre, H. I. Lin, W. L. Chen, Y. M. Chang, A. Rozhin, Y. T. Hsu, Y. F. Chen, R. Sankar, F. C. Chou, C. T.e Liang, *Nanoscale* **2020**, *12*, 18269.

[46] C. M. Raghavan, T. P. Chen, S. S. Li, W. L. Chen, C. Y. Lo, Y. M. Liao, G. Haider, C. C. Lin, C. C. Chen, R. Sankar, Y. M. Chang, F. C. Chou, C. W. Chen, *Nano Lett.* **2018**, *18*, 3221.

[47] J. X. Shen, X. Zhang, S. Das, E. Kioupakis, C. G. Van de Walle, *Adv. Energy Mater.* **2018**, *8*, 1801027.

[48] M. Roknuzzaman, J. A. Alarco, H. Wang, A. Du, T. Tesfamichael, K. (Ken) Ostrikov, *Comput. Mater. Sci.* **2019**, *169*, 109118.

[49] H. Yokoyama, S. D. Brorson, *J. app* **2012**, *66*, 4801.

[50] L. A. Coldren; S. W. Corzine; M. L. Masanovic, *Diode Lasers and Photonic Integrated Circuits*, John Wiley & Sons, Ltd, **2012**.

[51] K. L. Van Der Molen, A. P. Mosk, A. Lagendijk, *Phys. Rev. A – At. Mol. Opt. Phys.* **2006**, *74*, https://doi.org/10.1103/physreva.74.053808.

[52] N. Caselli, A. Consoli, Á. M. Mateos Sánchez, C. López, *Optica* **2021**, *8*, 193.

[53] N. Bachelard, S. Gigan, X. Noblin, P. Sebbah, *Nat. Phys.* **2014**, *10*, 426.

[54] J. Yi, Y. Yu, J. Shang, X. An, B. Tu, G. Feng, S. Zhou, *Opt. Express* **2016**, *24*, 5102.

[55] I. B. Dogru-Yuksel, M. Han, G. Pirnat, E. S. Magden, E. Senses, M. Humar, S. Nizamoglu, *APL Photonics* **2020**, *5*, 106105.

[56] J. Liu, P. D. Garcia, S. Ek, N. Gregersen, T. Suhr, M. Schubert, J. Mørk, S. Stobbe, P. Lodahl, *Nat. Nanotechnol.* **2014**, *9*, 285.

[57] S. Schönhuber, M. Brandstetter, T. Hisch, C. Deutsch, M. Krall, H. Detz, A. M. Andrews, G. Strasser, S. Rotter, K. Unterrainer, *Optica* **2016**, *3*, 1035.

[58] H. Cao, Y. G. Zhao, H. C. Ong, S. T. Ho, J. Y. Dai, J. Y. Wu, R. P. H. Chang, *Appl. Phys. Lett.* **1998**, *73*, 3656.

[59] L. Ye, F. Li, C. Lu, Z. Cheng, G. Hu, Y. Lu, Y. Cui, *Nanophotonics* **2017**, *7*, 473.

[60] Y. Yao, Z. Yang, J. Hwang, H. Su, J. Haung, T. Lin, J. Shen, M. Lee, M. Tsai, Y. Lee, *Adv. Opt. Mater.* **2017**, https://doi.org/10.1002/adom.201600746.

[61] R. Zhao, Z. Gu, P. Li, Y. Zhang, Y. Song, *Adv. Mater. Technol.* **2021**, *2101124*, 2101124.

[62] Y. Chen, J. Herrnsdorf, B. Guilhabert, Y. Zhang, I. M. Watson, E. Gu, N. Laurand, M. D. Dawson, *Opt. Express* **2011**, *19*, 2996.

[63] X. Zhang, S. Yan, J. Tong, X. Shi, S. Zhang, C. Chen, Y. Y. Xiao, C. Han, T. Zhai, *Nanophotonics* **2020**, *9*, 935.

[64] A. O. Murzin, B. V. Stroganov, C. Günnemann, S. Ben Hammouda, A. V. Shurukhina, M. S. Lozhkin, A. V. Emeline, Y. V. Kapitonov, *Adv. Opt. Mater.* **2020**, *8*, 2000690.

[65] W. Gao, T. Wang, J. Xu, P. Zeng, W. Zhang, Y. Yao, C. Chen, M. Li, S. F. Yu, *Small* **2021**, *17*, 2103065.

[66] L. Hou, Y. Wang, X. Liu, J. Wang, L. Wang, X. Li, G. Fu, S. Yang, *J. Mater. Chem. C* **2018**, *6*, 8770.

[67] C. Zhu, X. Niu, Y. Fu, N. Li, C. Hu, Y. Chen, X. He, G. Na, P. Liu, H. Zai, Y. Ge, Y. Lu, X. Ke, Y. Bai, S. Yang, P. Chen, Y. Li, M. Sui, L. Zhang, H. Zhou, Q. Chen, *Nat. Commun.* **2019**, *10*, 815.

[68] M. Wang, Z. Ni, X. Xiao, Y. Zhou, J. Huang, *Chem. Phys. Rev.* **2021**, *2*, 031302.

[69] Q. Tu, I. Spanopoulos, S. Hao, C. Wolverton, M. G. Kanatzidis, G. S. Shekhawat, V. P. Dravid, *ACS Energy Lett.* **2019**, *4*, 796.

[70] M. Fahim, I. Firdous, S.-W. Tsang, W. A. Daoud, *Nano Energy* **2022**, *96*, 107058.

[71] J. Rodríguez-Romero, J. Sanchez-Diaz, C. Echeverría-Arrondo, S. Masi, D. Esparza, E. M. Barea, I. Mora-Seró, *ACS Energy Lett.* **2020**, *5*, 1013.